



# Free-templated synthesis of N-doped PtCu porous hollow nanospheres for efficient ethanol oxidation and oxygen reduction reactions

XiaShuang Luo, CeHuang Fu, ShuiYun Shen, LiuXuan Luo<sup>\*</sup>, JunLiang Zhang<sup>\*</sup>

*Institute of Fuel Cells, Key Laboratory for Power Machinery and Engineering of MOE, School of Mechanical Engineering, Shanghai Jiao Tong University, Shanghai 200240, China*



## ARTICLE INFO

### Keywords:

Pt-based hollow nanospheres  
Ultrathin shells  
Kirkendall effect  
Ethanol oxidation reaction  
Oxygen reduction reaction

## ABSTRACT

Hollow metal-based nanoparticles usually possess improved electrocatalytic properties, but challenge in their tedious and complicated synthetic protocols. In this paper, a one-step template-free method is newly developed, whereby the N-doped PtCuCo polycrystalline nanospheres can be spontaneously transformed to the N-doped PtCuCo porous hollow nanospheres. Specifically, the Kirkendall voids form with the rapid removal of transition metals in the starting nanoparticles by a special diffusion–oxidation–complexation effect. The N-doped PtCu hollow nanospheres with ultrathin porous shells are formed after removing the surface oxides. A large electrochemical surface area of  $97.9 \text{ m}^2 \text{ g}_{\text{Pt}}^{-1}$  is established with the formation of abundant open channels in the hollow nanospheres. With the synergistic effect of the introduction of Cu, N components and the high Pt utilization, the N-doped PtCu porous hollow nanospheres demonstrate greatly enhanced electrocatalytic mass activities of  $2.14 \text{ A mg}_{\text{Pt}}^{-1}$  and  $1.42 \text{ A mg}_{\text{Pt}}^{-1}$  toward ethanol oxidation and oxygen reduction reactions, respectively.

## 1. Introduction

Seeking environmentally friendly energy technologies has become one of the key research issues toward energy crisis. Fuel cells are the promising alternatives to traditional energy-conversion devices due to their high efficiency, low emissions, and renewable fuel resources [1]. Among various types of fuel resources, ethanol has displayed the advantages of the convenient production, storage, and transportation [2]. As practical applications, direct ethanol fuel cells (DEFCs) have consequently drawn great attention in recent years [3,4]. However, the kinetically sluggish anodic ethanol oxidation reaction (EOR) and cathodic oxygen reduction reaction (ORR) are the pressing issues that need to be addressed in DEFCs. Therefore, more active electrocatalysts must be explored to facilitate the corresponding electrocatalytic processes [5–8].

Pt usually shows the superior catalytic nature in the specific field of electrocatalysis. Nevertheless, further reducing the usage of scarce Pt is still desirable. Progresses in electrochemical reaction mechanisms uncover that appropriately arranged local coordination environment plays an extraordinary role in boosting the reaction performance by modifying the Pt electronic structure [9,10]. For example, alloying Pt with other non-noble elements is an effective strategy to improve the

electrocatalytic activity towards both EOR and ORR [11–14]. More attractively, the intrinsic activity of those Pt-based nanoalloys is also morphology-dependent. Great efforts have been dedicated to synthesizing well-designed nanostructures so as to ideally maximize the Pt utilization [15–19]. Among various morphologies, hollow or porous structures possessing high atomic utilization, plentiful exposed catalytic sites, abundant available edges and corners as well as high mass-transfer rate have drawn intensive attention [20]. Recently, Han et al. [4] generated the porous trimetallic Pt–Rh–Cu cubic nanoboxes by the galvanic reaction strategy using  $\text{Cu}_2\text{O}$  nanocubes as template, which presented an enhanced activity of  $4090 \text{ mA mg}_{\text{Pt+Rh}}^{-1}$  for the EOR. It was observed that the hollow and porous structure provided mass-transfer channels while the participation of Rh and Cu promoted the C–C bond cleavage in the EOR process. Tian et al. [21] synthesized the bunched Pt–Ni alloy nanocages through the selectively removal of Ni species in the 1D Pt–Ni bunched nanospheres. Owing to the induced strain/ligand effects of Pt–Ni alloy and the exposure of plentiful accessible active sites, the bunched Pt–Ni nanocages demonstrated an improved ORR mass activity of  $3.52 \text{ A mg}_{\text{Pt}}^{-1}$ .

So far, to effectively avoid damaging the formed shells via conventional hard-template methods, sacrificial-template methods based on the Kirkendall effect, Ostwald ripening, galvanic replacement, and/or

\* Corresponding authors.

E-mail addresses: [luo\\_liuxuan@163.com](mailto:luo_liuxuan@163.com) (L. Luo), [junliang.zhang@sjtu.edu.cn](mailto:junliang.zhang@sjtu.edu.cn) (J. Zhang).

selective chemical etching have been widely explored for generating the inner cavities [22–26]. Besides, some intermediates with certain composition or structure were developed for the synthesis of hollow–nanostructure materials. For example, Wei et al. [27] reported a series of Pt–Co alloy hollow spheres by co-reducing  $\text{Pt}^{4+}$  and the amorphous Co–B–O complex. The as-synthesized flower-like Co–B–O complex was regarded as the structure-directing seeds in the sequential reduction. Han et al. [28] prepared the Ni–Co Prussian-blue-analog (PBA) nanocages by chemical-etching the heterogeneous solid Ni–Co PBA nanocubes. The interior cores rich in defects were selectively etched by ammonia in a faster rate, resulting in the formation of the cavities. Unfortunately, such template-assisted process still encounters many challenges in the controlled synthesis of shaped templates/cores, heterogeneous nucleation, and tedious structural evolution process. Therefore, it is suggestive to develop a more effective and facile self-reconstruction process for carving general homogeneous materials.

Dealloying transition metals from transition metal-enriched Pt-based bimetallic nanoparticles could lead to the formation of voids in homogeneous materials [29]. Gan et al. [30] further uncovered that the voids formation relies on the dealloying gaseous atmosphere in  $\text{PtNi}_3$  nanoparticles. Generally, the energetically favorable surface compositions of Pt-based nanoparticles vary under different gaseous atmospheres, and the transition metals are predicted to be segregated from the homogeneous bulk in  $\text{O}_2$  [31,32]. As a result, the Ni leaching rate in  $\text{PtNi}_3$  was accelerated and became faster than the Pt surface diffusion rate in  $\text{O}_2$ . Compared with the solid core–shell structure formed in  $\text{N}_2$ , the voids were generated with the continuous dealloying deep into the bulk to form the spongy structure in  $\text{O}_2$ .

Inspired by the gaseous-driven restructuring effect, we herein establish a counter-diffusion of Pt and transition metals in the N-doped PtCuCo polycrystalline nanospheres (N–PtCuCo PNSs) through the continuous dissolution of transition metals under oxygenic atmosphere. Based on the Kirkendall effect, the hollow structure is synthesized due to the higher outward diffusion rate of transition metals. A special oxidation–complexation effect of transition metals for chemical dealloying is conformed. Unlike the typical template-assisted methods, the synthesis of hollow nanospheres in our case relies on a spontaneous self-reconstruction rather than the pre-fabricating sacrificial templates or heterogeneous structures, which can thus be termed as the template-free method. The resultant N-doped  $\text{Pt}_7\text{Cu}$  porous hollow nanospheres (N–Pt<sub>7</sub>Cu PHNSs) have about 6–7 at. layers in the shell thickness, together with abundant open porous channels, providing large accessible active surfaces. Benefiting from both the structural and compositional effects, the electrocatalytic mass activities measured for the EOR and ORR are respective 5.02 and 13.42 times those of commercial Pt/C.

## 2. Experimental section

### 2.1. Synthesis of the N–Pt<sub>7</sub>Cu PHNSs and the N–PtCu PYSNSs

To synthesize the N–Pt<sub>7</sub>Cu PHNSs, 35 mg of  $\text{Pt}(\text{acac})_2$  (Sigma–Aldrich, 97%) was dispersed into an argon (Ar)-saturated solution containing 40 mL of ethylene glycol (EG, Aladdin, 99%) and 160  $\mu\text{L}$  of Poly dimethyl diallyl ammonium chloride (PDDA, Damas–Beta, mw 10w, aq. 35 wt 100–200cp) by sonication. The resulting mixture was then heated to 130 °C under an Ar flow in a three-neck flask. Subsequently, another 8 mL of Ar-saturated EG mixture containing 4 mg  $\text{mL}^{-1}$   $\text{Cu}(\text{acac})_2$  (Sigma–Aldrich, 97%) and 5 mg  $\text{mL}^{-1}$   $\text{Co}(\text{acac})_2$  (Sinopharm Chemical Reagent, 99%) was slowly injected into the three-neck flask under continuous stirring. After the injection, the three-neck flask was sealed by vacuum grease and kept at 130 °C for 90 min. All the above-mentioned experimental operations should be conducted in an Ar flow. Finally, the gaseous atmosphere was quickly changed from Ar to air by using an air pump before the resulting mixture was cooled to the room temperature. The as-synthesized N-doped PtCuCo porous hollow nanospheres (N–PtCuCo PHNSs) were supported onto the XC-72 carbon

powders and washed repeatedly with the solution of ethanol (EtOH, Sinopharm Chemical Reagent, 99%) and ultra-pure water. After a drying process, the as-obtained product powers were stirred in a 40% acetic acid (Sigma–Aldrich, 99%) solution at 80 °C for 1 h to synthesize the N–Pt<sub>7</sub>Cu PHNSs.

For the synthesis of the N-doped PtCu porous yolk–shell nanospheres (N–PtCu PYSNSs), 35 mg of  $\text{Pt}(\text{acac})_2$  was dispersed into an Ar-saturated solution containing 40 mL of EG and 80  $\mu\text{L}$  of PDDA by sonication. The resulting mixture was then heated to 160 °C under an Ar flow in a three-neck flask. Subsequently, another 8 mL of Ar-saturated EG mixture containing 6 mg  $\text{mL}^{-1}$   $\text{Cu}(\text{acac})_2$  was slowly injected into the three-neck flask under continuous stirring. After the injection, the three-neck flask was sealed by vacuum grease and kept at 160 °C for 90 min. Other subsequent operations were identical to the synthesis of the N–PtCuCo PHNSs.

### 2.2. Electrochemical measurements

All the electrochemical measurements were conducted on a CHI-660 potentiostat with a rotating disk electrode (RDE) system (Pine Research Instruments), using the glassy carbon as the working electrode (area: 0.196  $\text{cm}^2$ ) and the graphite rod as the counter electrode. The catalyst ink was prepared by ultrasonically dispersing the catalyst powders into a mixture of ethanol and 20 wt% Nafion solution (DuPont) with a volume ratio of 200:1. To paper a thin film of catalysts-coated working electrode, the obtained catalyst ink was then pipetted onto the glassy carbon rotating electrode polished with alumina, and dried under ambient condition. The calomel electrode as the reference electrode was calibrated in  $\text{H}_2$ -saturated 0.1 M  $\text{HClO}_4$  (Sigma–Aldrich, 70%) solution and 0.5 M  $\text{H}_2\text{SO}_4$  (Sinopharm, 98%) solution, respectively. All of the potentials used in this paper were converted to the reversible hydrogen electrode (RHE). The working electrodes with the Pt loading of 6  $\mu\text{g cm}^{-2}$  were activated by performing cyclic voltammetry (CV) sweeps between 0.02 and 1.1 V versus RHE at a scan rate of 0.5  $\text{V s}^{-1}$  in a  $\text{N}_2$ -saturated 0.1 M  $\text{HClO}_4$  solution.

After obtaining stable CV curves, another 10 cycles of CV curves were recorded in the same potential range at 20  $\text{mV s}^{-1}$ . The electrochemical surface area (ECSA) was evaluated by the hydrogen underpotential deposition assuming the hydrogen adsorption constant of 210  $\mu\text{C cm}^{-2}$ . The ORR polarization curves were recorded in an  $\text{O}_2$ -saturated 0.1 M  $\text{HClO}_4$  solution by linear sweep voltammetry (LSV) sweeps from 0.2 to 1.1 V versus RHE at 10  $\text{mV s}^{-1}$  with a rotation rate of 1600 rpm. For the ORR catalytic activity, the kinetic current at 0.9 V versus RHE was calculated by the Koutecky–Levich equation, and normalized by the ECSA and the Pt loading, respectively. The EOR measurement was conducted in a 0.5 M  $\text{H}_2\text{SO}_4$  + 1.0 M EtOH solution by the CV between 0.025 and 1.165 V at 20  $\text{mV s}^{-1}$  under  $\text{N}_2$  atmosphere. The electrochemical adsorption contribution from the  $\text{H}_2\text{SO}_4$  solution was corrected by deducting the measured CV currents in a 0.5 M  $\text{H}_2\text{SO}_4$  solution at the same scan rate and potential region.

### 2.3. Characterization

Transmission electron microscope (TEM) and high resolution–transmission electron microscope (HR–TEM) images were collected on a JEOL 2100 F field emission microscope and a FEI Talos F200X G2 TEM. High angle annular dark field-scanning transmission electron microscopy (HAADF–STEM) images and energy dispersive X-ray spectroscopy (EDX) mappings were acquired on a JEOL JEM-ARM 200 F with spherical aberration correction and a FEI Talos F200X G2 TEM. For observation, the catalysts were ultrasonically dispersed in ethanol and applied to aurum grids. An iCAP6300 inductively coupled plasma (ICP) Optical was used for compositional analyses. X-ray photoelectron spectroscopy (XPS) measurements were conducted on an AXIS UltraDLD spectrometer.

## 2.4. Computational details

The density functional theory (DFT) calculation was performed by the Vienna ab initio Simulation Program (VASP) [33–36]. The PBE functional with projector augmented wave pseudo-potential was used in all the calculations [37,38]. A Gaussian smearing technique was applied with a smearing parameter of  $k_{\text{BT}} = 0.1$  eV for the fractional occupation of the one-electron energy levels to accelerate the SCF convergence, and the calculated energies were extrapolated to  $k_{\text{BT}} = 0$  eV. The DFT-D3 method with Becke-Jonson damping was applied to describe the van der Waals interactions resulting from the dynamical correlations between the fluctuating charge distributions.

The crystal models were sampled with the  $11 \times 11 \times 11$  Monkhorst-Pack grids. After the convergence tests ( $< 1$  meV atom $^{-1}$ ). The slab calculations were sampled by a Monkhorst-Pack k-point net of  $5 \times 5 \times 1$  with the cutoff energy of 500 eV, and the molecule calculations were sampled by the Gamma point with the cutoff energy of 500 eV. The representative (111) surface was considered in calculation. All of the slab models consisted of 4 layers of metal atoms. The top two layers were relaxed in the calculation. The dipole correction was used along the z-direction and a vacuum of 15 Å was applied. In the Pt<sub>7</sub>Cu model, the Cu atoms in the top two layers were replaced by Pt atoms because of the acid leaching. In the N-Pt<sub>7</sub>Cu slab, the N atom was doped in the subsurface according to the stability test, which was also reported in previous works [39,40]. The top and side views of the three clean slabs are presented in Fig. S6. Other details are collected in the supplementary material.

## 3. Results and discussion

### 3.1. Evolution process

The N-PtCuCo PHNSs are synthesized by rapidly dealloying the solid N-PtCuCo PNSs in the reaction solution. The structural evolution of the solid N-PtCuCo PNSs proceeds immediately after the removal of the inert gas (Experimental Section). It is observed that the reaction mixture changes from purplish-red to black in few minutes with the formation of hollow structures. On this account, investigating the representative intermediates at different evolution stages becomes rather challenging. To further reveal the structural transformation process, some mother liquor-capped N-PtCuCo PNSs are dispersed in ethanol and kept under ambient conditions for obtaining the partly dealloyed sample. The collected structural evolution results are shown in Fig. 1. A continuous decrease in particle size can be observed during the structural transformation. As investigated by TEM and HR-TEM (Fig. 1a), the starting N-PtCuCo PNSs are comprised of numerous crystalline grains. The (111) and (200) lattice spacings recorded from the inner region are 0.204/0.206 nm and 0.174/0.177 nm, which are close to the Co or Cu interplanar spacing. It is noted that the N-PtCuCo PNSs are inevitably oxidized during centrifugation, evidenced by the estimated lattice spacing of 0.238 nm near the surface. Besides, an ultrathin organic film can be observed on the particle surfaces. As the dealloying continue, the thickness of the coated organic film increases with the appearance of cavity (Fig. 1b). Simultaneously, a Pt-rich phase with the (111) lattice spacing of 0.216 nm forms in the partly dealloyed sample. It is suggested that Cu and Co with the high oxygen affinity are oxidized and dissolved from the starting polycrystalline nanoparticles by forming soluble metal

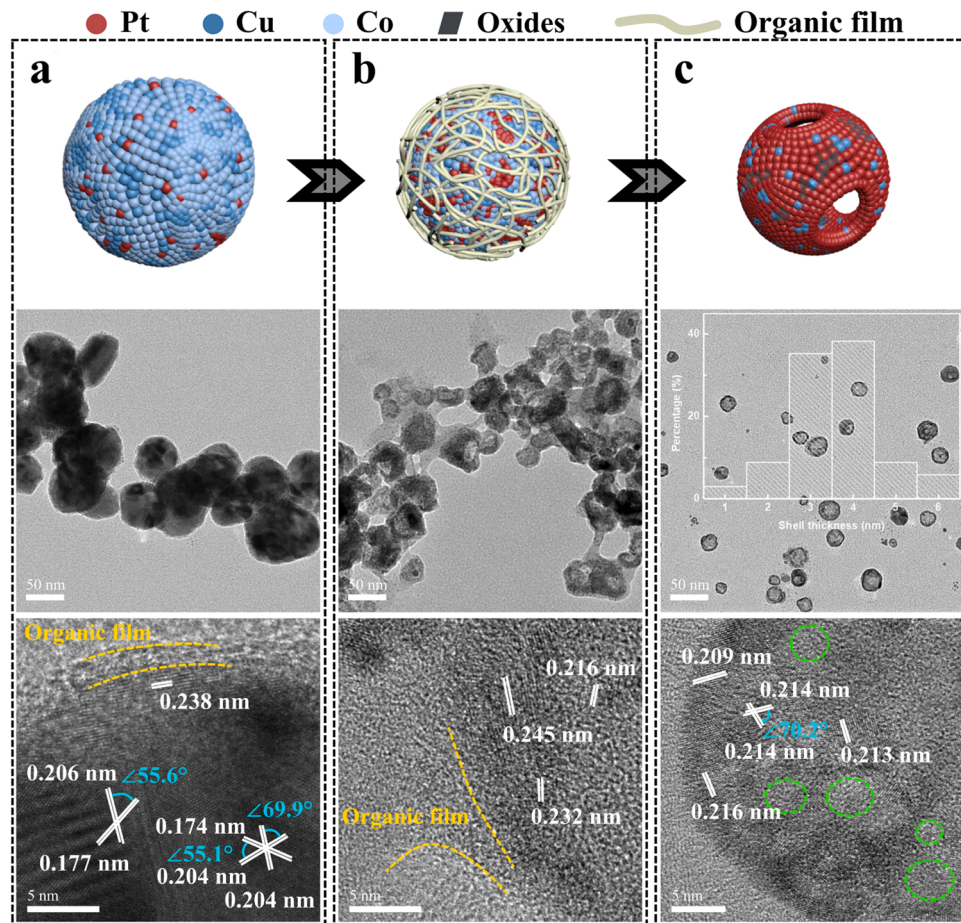


**Fig. 1.** Schematic illustrations as well as the corresponding TEM and HR-TEM images of (a) the N-PtCuCo PNSs, (b) the partly dealloyed N-PtCuCo PNSs, and (c) the N-PtCuCo PHNSs.

complexes with the mother liquor, leading to the formation of the Pt-rich phase. The similar oxidation followed by the dissolution of Ni in PtNi alloys has also been observed in the oleylamine system [5]. Fig. 1c depicts the typical TEM and HR-TEM images of the N–PtCuCo PHNSs resulting from the rapid dealloying. The formed nanoparticles show the hollow morphology with a highly dense nanopores (indicated by green circles). The corresponding size distribution histogram illustrates that, although those hollow nanospheres vary in cavity diameter, the ultrathin shells formed with a uniform thickness of ~1.52 nm. Compared with the starting N–PtCuCo PNSs, the (111) lattice spacings increase to 0.209–0.216 nm in the N–PtCuCo PHNSs, indicating a Pt-rich bulk composition. Interestingly, combining with the low-resolution TEM image shown in Fig. S1a, the organic complexes are observed to separate from the particle surfaces and assemble in the solution with the formation of the N–PtCuCo PHNSs.

The compositional transformation at the atomic scale is further characterized via the STEM. Fig. 2 depicts the HAADF-STEM images and the STEM-EDX elemental mapping results of the partly dealloyed N–PtCuCo PNSs. The atomic-resolution HAADF-STEM image of the unoxidized region with a (200) lattice spacing of 0.179 nm is shown in Fig. 2b. It is observed that the brighter dots of single Pt atoms are dispersed as the solute atoms in the N–PtCuCo PNSs. The unexpected Pt-deficient bulk composition should suggest a strong coordination between  $\text{Pt}^{2+}$  and the reaction solution as  $\text{Pt}^{2+}$  has a greater tendency to attract electrons than  $\text{Cu}^{2+}$  or  $\text{Co}^{2+}$ . As for the oxidized region shown in Fig. 2c, Pt atoms are found to segregate under the oxide layers, suggesting an inward diffusion of Pt atoms for forming the Pt-rich shells. This relocation process may also account for the constantly decreasing particle size observed by the TEM. In Pt–3d metal alloys, this energetically favorable outward diffusion of 3d metal atoms via the displacement under oxidation environments was frequently reported in previous researches [41,42]. Apart from displacement, it is believed that a large portion of Cu and Co atoms in the N–PtCuCo PNSs can straightforwardly reach the particle surfaces, leaving the highly dense nanopores on the

shells. Although those differently oriented crystalline grains slightly vary in the lattice spacing, the corresponding elemental distribution mappings in Fig. 2d–f reveal a homogeneous distribution of Pt, Cu, and Co in the N–PtCuCo PNSs. A CuCo-rich bulk composition is also confirmed, in accordance with the above lattice spacing analysis. Moreover, a certain ratio of N is introduced in the nanoparticles, indicating the decomposition of PDDA. The organic film derived from the complexation between  $\text{Cu}^{2+}/\text{Co}^{2+}$  and mother liquor is also clear in the STEM images. From Fig. 2a and d, plenty of small Pt-rich nanoparticles detached from the N–PtCuCo PNSs can be found in the organic film. It is noted that those small Pt-rich nanoparticles are hardly observed in the organic complex formed with the formation of the N–PtCuCo PHNSs (Fig. S1b). The main reason is that the partly dealloyed sample is obtained under a low temperature. It is noted that the dealloying temperature is a crucial parameter in the restructuring. As shown in Fig. S2, decreasing the dealloying temperature to 20 °C increases the surface defects and shells thickness in the final hollow nanospheres due to the limited atomic thermal motion. Some hollow nanospheres even detached in fragments after the dealloying at 20 °C.

### 3.2. Evolution mechanism

It is believed that the fabrication of the porous hollow structure follows a mechanism based on the Kirkendall effect, in which the cavity formation depends on the difference in counter-diffusing rate. In brief, the outward diffusion of Cu and Co driven by the oxidation results in the formation of the initial Cu–Co oxides–Pt surfaces structure. Sequentially, a sustaining dissolution–diffusion–oxidation procedure of Co and Cu atoms proceeds on the surfaces, accompanied by a Pt inward segregation. Compared with Pt, the diffusion rates of Co and Cu are higher since part of Co and Cu atoms can straightforwardly reach the surface in those Pt-deficient nanoparticles. As a result, the continuous outward net flows of Cu and Co species leads to the generation of the Kirkendall voids.

The polycrystalline structure is vital to the successful realization of

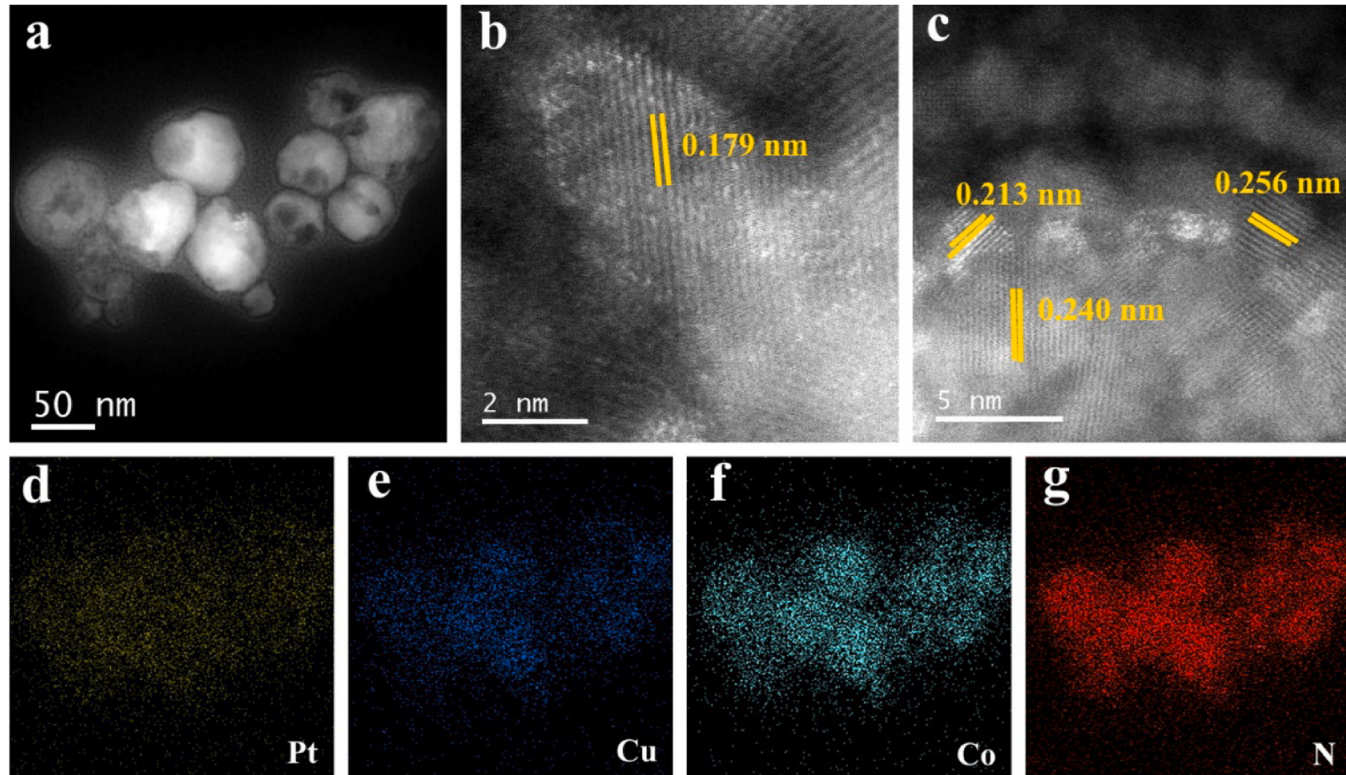


Fig. 2. (a–c) HAADF-STEM images and (d–f) STEM EDX-mappings of the partly dealloyed N–PtCuCo PNSs.

the Kirkendall voids. For comparison, the N-doped PtCu core-shell nanospheres (N-PtCu CSNSs) with higher alloying degree inside are employed as the starting materials in our template-free method. According to Fig. 3a–c, the contrast variations within the N-PtCu CSNSs (indicated by green circles) can be observed under both TEM and phase contrast HR-TEM, suggesting different nanostructures. The HR-TEM images illustrate continuous lattice fringes in the core regions, while the measured lattice spacings of both cores and shells match those of Cu-rich phase. It is thus believed that the contrast variations originate from the higher alloying degree inside. The TEM, HAADF-STEM images and the STEM-EDX elemental mapping results of the partly dealloyed N-PtCu CSNSs are presented in Fig. S3. From Fig. S3b–d, the Kirkendall voids (indicated by yellow arrows) form in the polycrystalline shell regions with dealloying.

After the rapid dealloying, the existing core in the starting N-PtCu CSNSs is retained to form the inner Cu-rich yolk structure, while the polycrystalline outer part undergoes a structural transformation to form the Pt-rich shell structure (Fig. 3d–f, the N-doped PtCu yolk-shell nanospheres, N-PtCu YSNSs). Similar to the N-PtCuCo PNSs, the decreasing particle size, oxidation-complexation of Cu as well as Pt-inward segregation are also observed in the polycrystalline shell regions. It is presumed that a pipe diffusion network can be established along the erratic twinning boundaries in the polycrystalline nanoparticle [43], which significantly enhance the counter-diffusion.

### 3.3. Catalysts characterization

The fine structure of the N-PtCuCo PHNSs is also investigated by the STEM. The atomic-resolution HAADF-STEM image presented in Fig. 4a suggests the highly dense nanopores in the shells, which is in accordance

with the HR-TEM image. EDX elemental mapping results confirm that Pt, Cu, Co, and N are homogeneously distributed in the ultrathin porous shells (Fig. 4b–e). Compared with the starting polycrystalline nanoparticles, the bulk composition examined by EDX changes from the Pt-deficient to the Pt-rich. Simultaneously, a Co-rich complex forms with the structural and compositional transformation beside the N-PtCuCo PHNSs, as observed in Fig. 4d. Detailed electronic structures characterized by XPS (Fig. S4) illustrate that, after the rapid dealloying, Co is mainly in the oxidation state whereas a certain amount of Cu is still metallic. It is noted that the deconvoluted peaks located at 935.22 and 783.24 eV are ascribed to the metallic ions in the formed organic complex. Compared with the metal oxides (933.78 and 781.59 eV), the observed higher binding energies indicate a strong interaction between the metallic ions and the organic complex, which accounts for the spontaneous dissolution of the metal oxides. An acid pickling is subsequently applied to the N-PtCuCo PHNSs. With the removal of the metal oxides and the Co-rich complex, the atomic ratio of Pt to Cu is determined to be 7:1 by ICP while the atomic concentration of Co is found lower than the limit of detection. Combining with the XPS results, the preserved Cu atoms suggest a suppressed Cu dissolution rate compared with that of Co in the N-PtCuCo PNSs. From Fig. 4f, the average thickness of the N-Pt<sub>7</sub>Cu porous shells decreases to 1.42 nm (around 6–7 at. layers). Besides, no element segregation of N, Pt, or Cu is observed in the N-Pt<sub>7</sub>Cu PHNSs determined by STEM-EDX, as shown in Fig. S5.

The elemental analyses based on XPS are performed to identify the surface chemistries of the N-Pt<sub>7</sub>Cu PHNSs/C. The resulting high-resolution spectra from the Pt 4 f, N 1 s, and Cu 2p core level regions are collected in Fig. 5. The overlapping Cu 3p doublet located between the binding energies of 66–82 eV is deconvoluted before the analysis

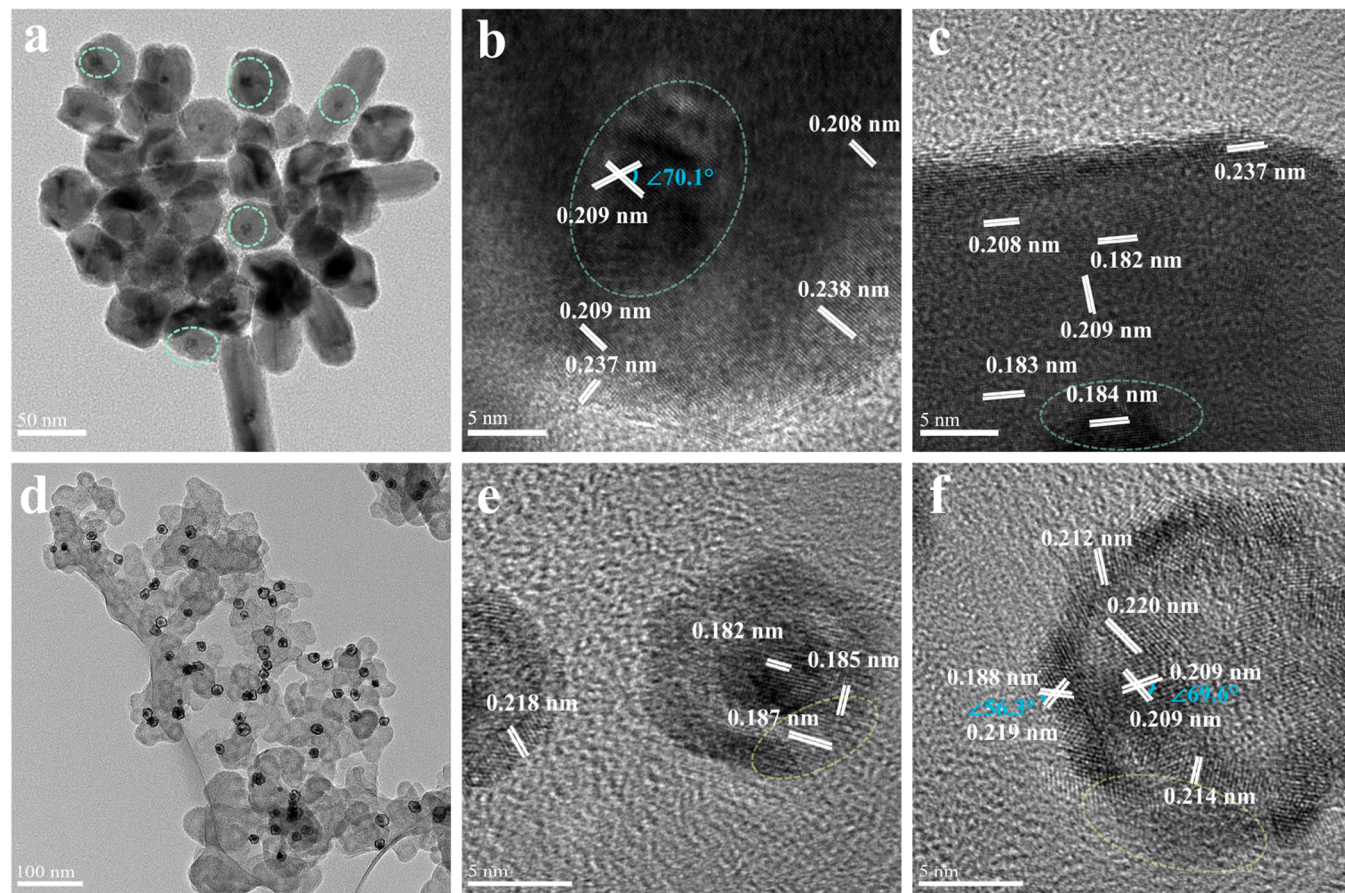


**Fig. 3.** (a) TEM and (b–c) HR-TEM images of the N-PtCu CSNSs, (d) TEM and (e–f) HR-TEM images of the N-PtCu YSNSs.

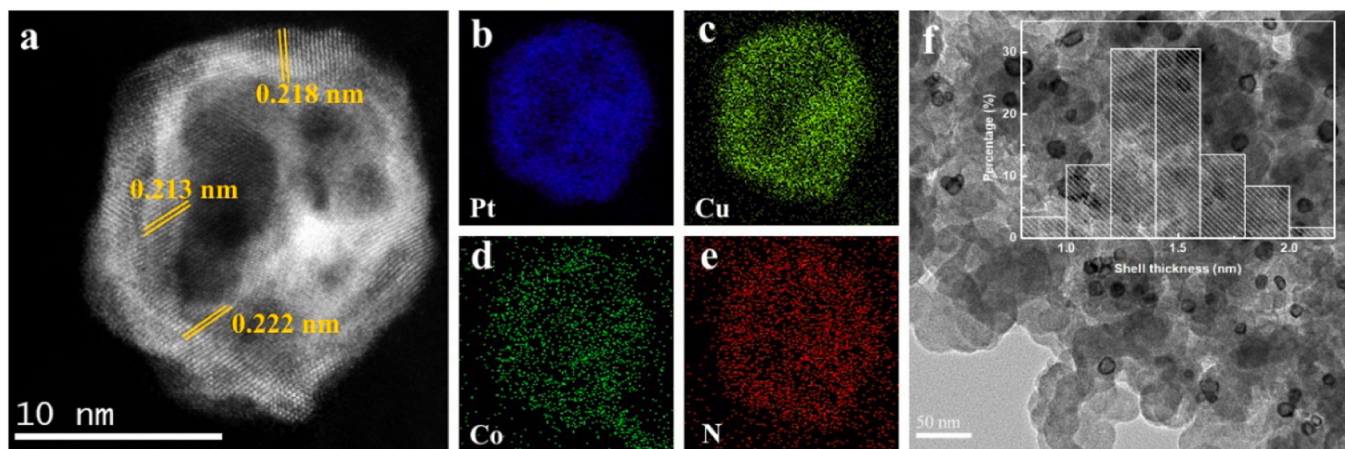


Fig. 4. (a) HAADF-STEM image and (b–e) STEM-EDXmappings of the N-PtCuCo PHNSs, (f) TEM image of the N-Pt<sub>7</sub>Cu PHNSs/C.

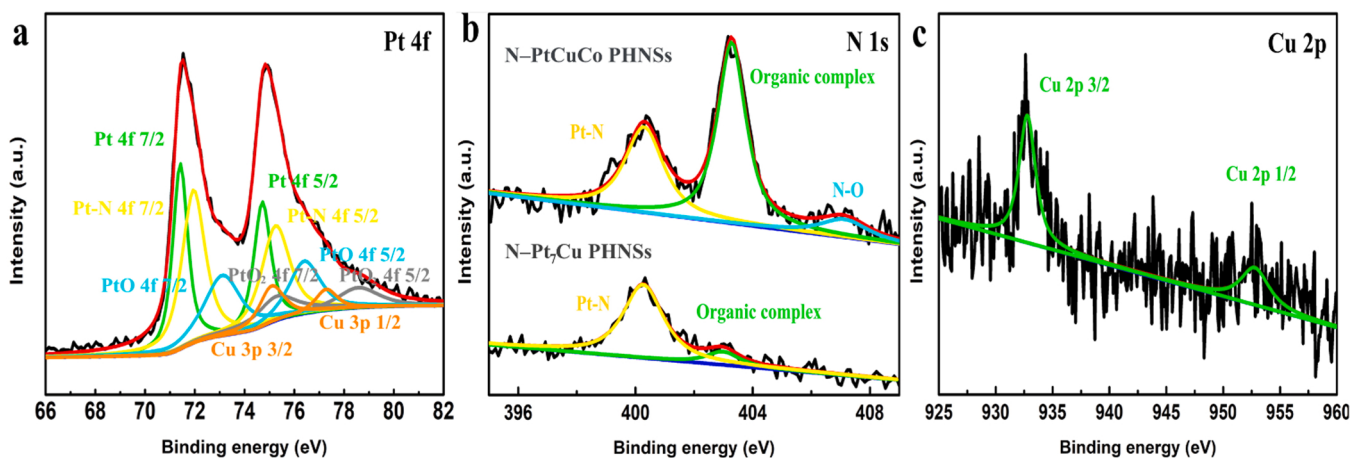


Fig. 5. (a) Pt 4 f XPS spectra of the N-Pt<sub>7</sub>Cu PHNSs, (b) N 1 s XPS spectra of the N-PtCuCo PHNSs and the N-Pt<sub>7</sub>Cu PHNSs, (c) Cu 2 p XPS spectra of the N-Pt<sub>7</sub>Cu PHNSs.

[44]. As shown in Fig. 5a, the Pt 4 f spectrum is further fitted with four doublets, corresponding to metallic Pt, Pt-N, PtO, and PtO<sub>2</sub>. It is seen that Pt atoms are partially oxidized during the structural transformation. For the metallic Pt, a positive shift of 0.31 eV is observed relative to that of pure Pt (71.1 eV), suggesting the change in Pt electronic structure. The deconvoluted peaks located at 71.95 eV and 75.25 eV are assigned to the 4 f<sub>7/2</sub> and 4 f<sub>5/2</sub> of Pt in Pt-N [39], whose binding energies are approximately 0.54 eV higher than that of the metallic Pt due to the strong interaction but much lower than that of PtO (73.10 and 76.40 eV). Fig. 5b presents the N 1 s spectra of the N-PtCuCo PHNSs and the N-Pt<sub>7</sub>Cu PHNSs. After the acid pickling, the deconvoluted peak located at 407.12 eV, which can be ascribed to the oxidation-state N, disappears while the intensity of the deconvoluted peak located at 403.28 eV significantly decreases. It is also known that the binding energy of N 1 s in the pure PDDA is 402 eV [45]. Therefore, the peak at 403.28 eV should be ascribed to the organic complex adsorbed on the catalysts and the positive shift of 1.28 eV may be attributed to the decomposition or oxidation of PDDA. Meanwhile, the preserved peak at 400.26 eV is assigned to the N 1 s of metal-N [46]. In the Cu 2p spectra, only one Cu state marked as the metallic Cu with a relatively lower content is observed, which is in consistent with pure Cu. It is thus believed that N atoms are mainly bonded with Pt.

### 3.4. Electrocatalytic properties and DFT calculation

The electrocatalytic ORR properties of the N-Pt<sub>7</sub>Cu PHNSs/C are

evaluated and compared to commercial Pt/C catalysts (TKK, 46.7%). As shown in Fig. 6a, with the introduction of Cu and N, the CV curves of the N-Pt<sub>7</sub>Cu PHNSs/C and commercial Pt/C vary with the adsorption/desorption peaks position. The ECSA is determined by the hydrogen underpotential deposition in a 0.1 M HClO<sub>4</sub> solution. As expected, the open structures extend the accessible surfaces of reactants, leading to a larger ECSA value of 97.9 m<sup>2</sup> g<sub>Pt</sub><sup>-1</sup>, which is 2.39 times that of commercial Pt/C. The polarization curves in Fig. 6b prove that the ORR activity of the N-Pt<sub>7</sub>Cu PHNSs/C is remarkably promoted, which reaches 1.45 mA cm<sup>-2</sup> and 1.42 A mg<sub>Pt</sub><sup>-1</sup> in area-specific and mass-specific activity, respectively. Fig. 6d presents the ORR energy profiles on the (111) facets of the pure Pt, the Pt<sub>7</sub>Cu, and the N-Pt<sub>7</sub>Cu by the DFT calculation. At U = 1.23 V, the highest reaction energy barrier on the pure Pt surface is 0.95 eV for ER<sub>4</sub>, which suggests that the formation of OH\* is the limiting reaction. Alloying Pt with Cu changes the rate-determining step to ER<sub>2</sub> (or the formation of OOH\*) with a decrease reaction energy barrier of 0.88 eV. This energy barrier further decreases to 0.83 eV after the doping of N element, which explains the enhanced ORR activity on the N-Pt<sub>7</sub>Cu PHNSs surfaces.

The d-band partial density of states (PDOS) of Pt atoms on the surfaces are calculated in Fig. S7. The d-band centers of the pure Pt, the Pt<sub>7</sub>Cu, and the N-Pt<sub>7</sub>Cu are -1.80, -1.94, and -1.70 eV, respectively. It is observed that the d-band center of Pt increases significantly after the N doping. According to the d-band center theory, the anti-bonding orbital would be filled with less electrons and the adsorption of intermediates should be intensified. The stronger adsorption of O<sub>2</sub> would

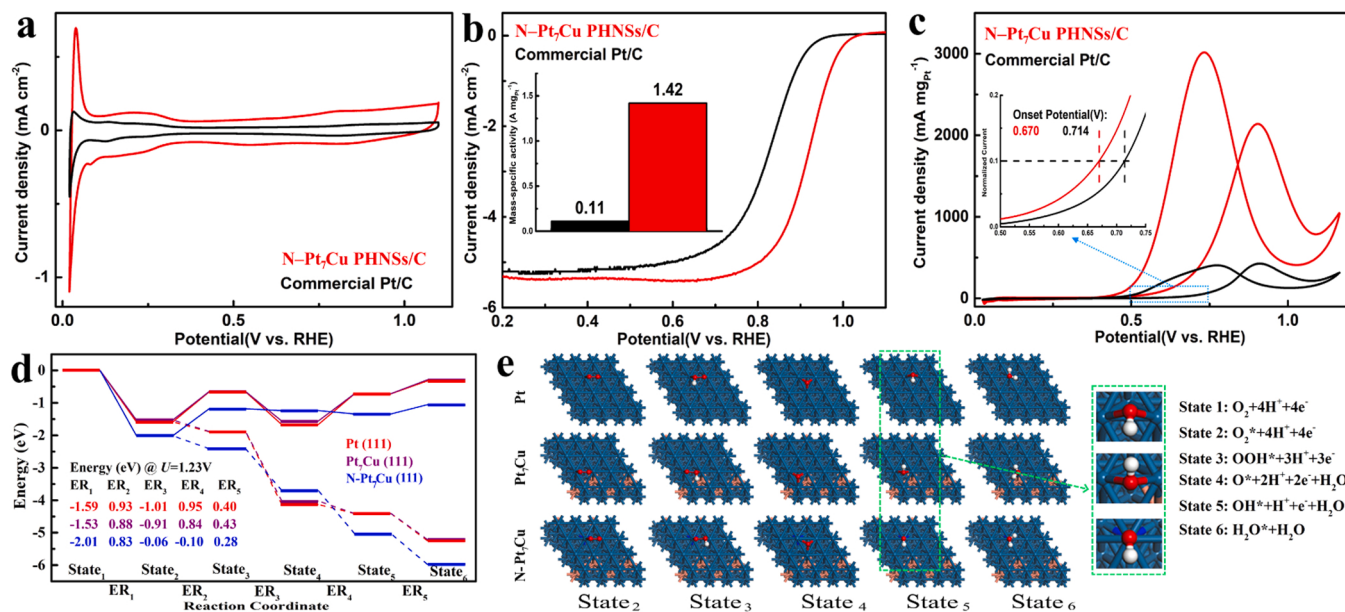


**Fig. 6.** (a) CV curves in  $N_2$ -saturated 0.1 M  $HClO_4$  solution at  $20\text{ mV s}^{-1}$ , (b) LSV curves in  $O_2$ -saturated 0.1 M  $HClO_4$  solution at  $10\text{ mV s}^{-1}$ , (c) CV curves in 0.5 M  $H_2SO_4$  + 1 M EtOH solution at  $20\text{ mV s}^{-1}$ , (d) the  $4e^-$  ORR energy profiles on the (111) facets of the pure Pt, the  $Pt_7Cu$ , and the N– $Pt_7Cu$  at 0 (dash line) and 1.23 V (solid line), (e) the top views of ORR intermediates.

increase the amount of anti-bonding electrons in the  $O=O$  bond, which promotes the breaking of the  $O=O$  bond and the formation of  $OOH^*$  [47]. Interestingly, it is found in Fig. 6e that the adsorbent structures of  $OH^*$  (state<sub>5</sub>) on the N– $Pt_7Cu$  is different from that on the pure Pt or the  $Pt_7Cu$ . As a result, the  $OH^*$  adsorption is stronger than the  $O^*$  adsorption, for which the formation of  $OH^*$  is promoted and ER<sub>4</sub> becomes an energetically favorable step on the N– $Pt_7Cu$ .

In addition to the ORR, the N– $Pt_7Cu$  PHNSs/C are also applied to the EOR. Fig. 6c shows the CV curves of the N– $Pt_7Cu$  PHNSs/C and the commercial Pt/C toward the EOR at  $20\text{ mV s}^{-1}$ . The forward scan peaks at 0.9 V (vs. RHE) for the N-doped hollow  $Pt_7Cu/C$  and 0.91 V for the commercial Pt/C can be assigned to the electro-oxidation of ethanol. The insert in Fig. 6c presents the onset potentials defined as the potentials at 10% of the forward peak currents of both catalysts. A negative shift of 44 mV indicates a lower EOR overpotential on the N– $Pt_7Cu$  PHNSs/C. The mass activity of the N– $Pt_7Cu$  PHNSs/C towards the EOR is calculated to  $2.14\text{ A mg}_{Pt}^{-1}$ , which is 5.02 times that of commercial Pt/C ( $0.427\text{ A mg}_{Pt}^{-1}$ ). Besides, a relatively high backward to forward peak current ratio is observed on the N– $Pt_7Cu$  PHNSs/C, indicating the faster regeneration of active sites during the backward scanning [48]. The comparison of the ORR and the EOR activities with some representative electrocatalysts is presented in Table S1.

#### 4. Conclusion

In conclusion, the N– $Pt_7Cu$  PHNSs with ultrathin shells are successfully synthesized through dealloying the N– $PtCuCo$  PNSs. As investigated through adjusting the dealloying degree, an unusual complexation is confirmed to constantly remove transition metal oxides as well as drive the counter-diffusion of Pt and transition metals in the N– $PtCuCo$  PNSs under the oxygenic atmosphere, yielding the hollow Pt-rich nanospheres. Owing to the formation of the additional transport channels along the grain boundaries, the counter-diffusion is enhanced for realizing the restructuring based on the Kirkendall effect, and the hollow structure is accessible in few minutes. Benefiting from the structural and compositional effects, the resulted N– $Pt_7Cu$  PHNSs/C possesses a large ECSA of  $97.9\text{ m}^2\text{ g}_{Pt}^{-1}$  while both the EOR and the ORR activity are also greatly promoted, which reach  $2.14\text{ A mg}_{Pt}^{-1}$  and  $1.42\text{ A mg}_{Pt}^{-1}$ , respectively.

#### CRediT authorship contribution statement

**Xiaoshuang Luo:** Conceptualization, Methodology, Investigation, Formal analysis, Writing – original draft. **Cehuang Fu:** Methodology, Investigation, Formal analysis. **Shuiyun Shen:** Supervision, Funding acquisition. **Liuxuan Luo:** Supervision, Writing – review & editing. **Junliang Zhang:** Conceptualization, Supervision, Writing – review & editing, Funding acquisition.

#### Declaration of Competing Interest

The authors declare that they have no known competing financial interests or personal relationships that could have appeared to influence the work reported in this paper.

#### Data Availability

Data will be made available on request.

#### Acknowledgements

This work was financially supported by the National Key Research and Development Program of China (2021YFB4001301), the National Natural Science Foundation of China (21975157) and the Science and Technology Commission of Shanghai Municipality (21DZ1208600). The electrochemical measurements were conducted with the help of Dr. Jiewei Yin from School of Mechanical Engineering, Shanghai Jiao Tong University.

#### Appendix A. Supporting information

Supplementary data associated with this article can be found in the online version at doi:10.1016/j.apcatb.2023.122602.

#### References

- [1] S.Y. Yang, D.J. Seo, M.R. Kim, M.H. Seo, S.M. Hwang, Y.M. Jung, B.J. Kim, Y.G. Yoon, B. Han, T.Y. Kim, Fast stack activation procedure and effective long-term storage for high-performance polymer electrolyte membrane fuel cell, *J. Power Sources* 328 (2016) 75–80.

- [2] A. Rabis, P. Rodriguez, T.J. Schmidt, Electrocatalysis for polymer electrolyte fuel cells: recent achievements and future challenges, *ACS Catal.* 2 (2012) 864–890.
- [3] V.K. Puthiyapura, D.J.L. Brett, A.E. Russell, W.F. Lin, C. Hardacre, Biobutanol as fuel for direct alcohol fuel cells—investigation of Sn-modified Pt catalyst for butanol electro-oxidation, *ACS Appl. Mater. Interfaces* 8 (2016) 12859–12870.
- [4] S.H. Han, H.M. Liu, P. Chen, J.X. Jiang, Y. Chen, Porous trimetallic PtRhCu cubic nanoboxes for ethanol electrooxidation, *Adv. Energy Mater.* 8 (2018), 1801326.10.
- [5] C. Chen, Y. Kang, Z. Huo, Z. Zhu, W. Huang, H.L. Xin, J.D. Snyder, D. Li, J. A. Herron, M. Mavrikakis, Highly crystalline multimetallic nanoframes with three-dimensional electrocatalytic surfaces, *Science* 343 (2014) 1339–1343.
- [6] F. Saleem, Z. Zhang, B. Xu, X. Xu, P. He, X. Wang, Ultrathin Pt–Cu nanosheets and nanocones, *J. Am. Chem. Soc.* 135 (2013) 18304–18307.
- [7] E.A. Monyoncho, S.N. Steinmann, C. Michel, E.A. Baranova, T.K. Woo, P. Sautet, Ethanol electro-oxidation on palladium revisited using polarization modulation infrared reflection absorption spectroscopy (PM-IRRAS) and density functional theory (DFT): why is it difficult to break the C–C bond? *ACS Catal.* (2016) 4894–4906.
- [8] H.A. Hansen, V. Viswanathan, J.K. Nørskov, Unifying kinetic and thermodynamic analysis of 2 e- and 4 e- reduction of oxygen on metal surfaces, *J. Phys. Chem. C* 118 (2014) 6706–6718.
- [9] V. Stamenkovic, B.S. Mun, K.J.J. Mayrhofer, P.N. Ross, N.M. Markovic, J. Rossmeisl, J. Greeley, J.K. Nørskov, Changing the activity of electrocatalysts for oxygen reduction by tuning the surface electronic structure, *Angew. Chem.* 45 (2010), 2815–2815.
- [10] S. Dai, T.H. Huang, X. Yan, C.Y. Yang, T.Y. Chen, J.H. Wang, X. Pan, K.W. Wang, Promotion of ternary Pt–Sn–Ag catalysts toward ethanol oxidation reaction: revealing electronic and structural effect of additive metals, *ACS Energy Lett.* 3 (2018) 2550–2557.
- [11] H. Liu, J. Li, L. Wang, Y. Tang, B.Y. Xia, Y. Chen, Trimetallic PtRhNi alloy nanoassemblies as highly active electrocatalyst for ethanol electrooxidation, *Nano, Research* 10 (2017) 3324–3332.
- [12] Z. Xu, Y. Wang, Effects of alloyed metal on the catalysis activity of Pt for ethanol partial oxidation: adsorption and dehydrogenation on Pt3M (M = Pt, Ru, Sn, Re, Rh, and Pd), *J. Phys. Chem. C* 115 (2011) 20565–20571.
- [13] Y. Liu, S. Liu, Z. Che, S. Zhao, X. Sheng, M. Han, J. Bao, Concave octahedral Pd@PdPt electrocatalysts integrating core-shell, alloy and concave structures for high-efficiency oxygen reduction and hydrogen evolution reactions, *J. Mater. Chem. A* 4 (2016) 16690–16697.
- [14] M. Escudero-Escobar, P. Malacrida, M.H. Hansen, U.G. Vej-Hansen, I. Chorkendorff, Tuning the activity of Pt alloy electrocatalysts by means of the lanthanide contraction, *Science* 352 (2016) 73–76.
- [15] M. Gong, Z. Deng, D. Xiao, L. Han, T. Zhao, Y. Lu, T. Shen, X. Liu, R. Lin, T. Huang, One-nanometer-thick Pt 3 Ni bimetallic alloy nanowires advanced oxygen reduction reaction integrating multiple advantages into one catalyst, *ACS Catal.* 9 (2019) 4488–4494.
- [16] C. Zhang, W. Sandorf, Z. Peng, Octahedral Pt2CuNi uniform alloy nanoparticle catalyst with high activity and promising stability for oxygen reduction reaction, *ACS Catal.* 5 (2015) 2296–2300.
- [17] X.Y. Liu, Y. Zhang, M.X. Gong, Y.W. Tang, T.H. Lu, Y. Chen, J.M. Lee, Facile synthesis of corallite-like Pt–Pd alloy nanostructures and their enhanced catalytic activity and stability for ethanol oxidation, *J. Mater. Chem. A* 2 (2014) 13840–13844.
- [18] J.E. Sulaiman, S. Zhu, Z. Xing, Q. Chang, M. Shao, Pt–Ni octahedra as electrocatalysts for the ethanol electro-oxidation reaction, *ACS Catal.* 7 (2017) 5134–5141.
- [19] M. Bao, L.S. Amiuu, T. Peng, W. Li, S. Liu, Z. Wang, Z. Pu, D. He, Y. Xiong, S. Mu, Surface evolution of PtCu alloy shell over Pd nanocrystals leads to superior hydrogen evolution and oxygen reduction reactions, *ACS Energy Lett.* 3 (2018) 940–945.
- [20] R. Jamil, M. Sohail, N. Baig, M.S. Ansari, R. Ahmed, Synthesis of hollow Pt–Ni nanoboxes for highly efficient methanol oxidation, *Sci. Rep.* 9 (2019) 15273.
- [21] X. Tian, X. Zhao, Y.Q. Su, L. Wang, B.Y. Xia, Engineering bunched Pt–Ni alloy nanocages for efficient oxygen reduction in practical fuel cells, *Science* 366 (2019) 850–856.
- [22] Y.D. Yin, R.M. Rioux, C.K. Erdonmez, S. Hughes, G.A. Somorjai, A.P. Alivisatos, Formation of hollow nanocrystals through the nanoscale Kirkendall effect, *Science* 304 (2004) 711–714.
- [23] R. Chattot, T. Asset, J. Drnec, P. Bordet, J. Nelayah, L. Dubau, F. Maillard, Atomic-scale snapshots of the formation and growth of hollow PtNi/C nanocatalysts, *Nano Lett.* 17 (2017) 2447–2453.
- [24] X. Xia, Y. Wang, A. Ruditskiy, Y. Xia, 25th anniversary article: galvanic replacement: a simple and versatile route to hollow nanostructures with tunable and well-controlled properties, *Adv. Mater.* 25 (2013) 6313–6333.
- [25] L. Shen, L. Yu, H.B. Wu, X.Y. Yu, X.W.D. Lou, Formation of nickel cobalt sulfide ball-in-ball hollow spheres with enhanced electrochemical pseudocapacitive properties, *Nat. Commun.* 6 (2015) 6694.
- [26] L. Yu, H.B. Wu, X. Lou, Self-templated formation of hollow structures for electrochemical energy applications, *Acc. Chem. Res.* 50 (2017) 293–301.
- [27] W.A. Min, H.A. Lei, B. Sha, B. Zea, B. Dla, A. Xz, A. Sw, Q. Zhi, K. Pei, Highly efficient Pt–Co alloy hollow spheres with ultra-thin shells synthesized via Co–B–O complex as intermediates for hydrogen evolution reaction, *J. Catal.* 381 (2020) 385–394.
- [28] Han Lei, Yu Xin-Yao, Wen Xiong, Lou, Formation of prussian-blue-analog nanocages via a direct etching method and their conversion into Ni–Co–mixed oxide for enhanced oxygen evolution, *Adv. Mater.* 28 (2016) 4601–4605.
- [29] M. Oezaslan, M. Heggen, P. Strasser, Size-dependent morphology of dealloyed bimetallic catalysts: linking the nano to the macro scale, *J. Am. Chem. Soc.* 134 (2012) 514–524.
- [30] L. Gan, M. Heggen, R. O’Malley, B. Theobald, P. Strasser, Understanding and controlling nanoporosity formation for improving the stability of bimetallic fuel cell catalysts, *Nano Lett.* 13 (2013) 1131–1138.
- [31] C.A. Menning, J.G. Chen, Regenerating Pt-3d-Pt model electrocatalysts through oxidation–reduction cycles monitored at atmospheric pressure, *J. Power Sources* 195 (2010) 3140–3144.
- [32] X. Luo, Y. Guo, H. Zhou, H. Ren, J. Zhang, Thermal annealing synthesis of double-shell truncated octahedral Pt–Ni alloys for oxygen reduction reaction of polymer electrolyte membrane fuel cells, *Front. Energy* 14 (2020) 767–777.
- [33] G. Kresse, J. Hafner, Ab initio molecular dynamics for liquid metals, *Phys. Rev. B* 47 (1993) 558–561.
- [34] G. Kresse, J. Hafner, Ab initio molecular-dynamics simulation of the liquid–metal–amorphous–semiconductor transition in germanium, *Phys. Rev. B* 49 (1994) 14251–14269.
- [35] G. Kresse, J. Furthmüller, Efficiency of ab-initio total energy calculations for metals and semiconductors using a plane-wave basis set, *Comput. Mater. Sci.* 6 (1996) 15–50.
- [36] G. Kresse, J. Furthmüller, Efficient iterative schemes for ab initio total-energy calculations using a plane-wave basis set, *Phys. Rev. B, Condens. Matter* 54 (1996) 11169–11186.
- [37] G. Kresse, D. Joubert, From ultrasoft pseudopotentials to the projector augmented-wave method, *Phys. Rev. B* 59 (1999) 1758–1775.
- [38] P. Blöchl, E. Blöchl, P. Blöchl, Projected augmented-wave method, *Phys. Rev. B* 50 (1994) 17953–17979.
- [39] M. Luo, J. Cai, J. Zou, Z. Jiang, G. Wang, X. Kang, Promoted alkaline hydrogen evolution by an N-doped Pt–Ru single atom alloy, *J. Mater. Chem. A* 9 (2021) 4941–4947.
- [40] Q. Chen, B. Wei, Y. Wei, P. Zhai, W. Liu, X. Gu, Z. Yang, J. Zuo, R. Zhang, Y. Gong, Synergistic effect in ultrafine PtNiP nanowires for highly efficient electrochemical hydrogen evolution in alkaline electrolyte, *Appl. Catal. B: Environ.* 301 (2022), 120754.
- [41] C. Menning, J.G. Chen, Thermodynamics and kinetics of oxygen-induced segregation of 3d metals in Pt-3d-Pt(111) and Pt-3d-Pt(100) bimetallic structures, *J. Chem. Phys.* 128 (2008), 164703.
- [42] S.H. Noh, M.H. Seo, J.K. Seo, P. Fischer, B. Han, First principles computational study on the electrochemical stability of Pt–Co nanocatalysts, *Nanoscale* 5 (2013) 8625–8633.
- [43] R.J. Borg, G.J. Dienes, *An Introduction to Solid State Diffusion*, Academic Press, 1988.
- [44] C.J. Powell, N.E. Erickson, T. Jach, Accurate determination of the energies of auger electrons and photo-electrons from nickel, copper, and gold, *J. Vac. Sci. Technol.* 20 (1982) 625.
- [45] S. Wang, D. Yu, L. Dai, Polyelectrolyte functionalized carbon nanotubes as efficient metal-free electrocatalysts for oxygen reduction, *J. Am. Chem. Soc.* 133 (2011) 5182–5185.
- [46] B. Kiefer, A. Serov, S. Kabir, K. Artyushkova, P. Atanassov, Binding energy shifts for nitrogen-containing graphene-based electrocatalysts – experiments and DFT calculations, surface and interface analysis: SIA: an international journal devoted to the development and application of techniques for the analysis of surfaces, *Interfaces Thin Films* 48 (2016) 293–300.
- [47] C. Fu, L. Luo, L. Yang, S. Shen, G. Wei, J. Zhang, Breaking the scaling relationship of ORR on carbon-based single-atom catalysts through building a local collaborative structure, *Catal. Sci. Technol.* 11 (2021) 7764–7772.
- [48] J.E. Sulaiman, S. Zhu, Z. Xing, Q. Chang, M. Shao, Pt–Ni octahedra as electrocatalysts for the ethanol electro-oxidation reaction, *ACS Catal.* 7 (2017) 5134–5141.